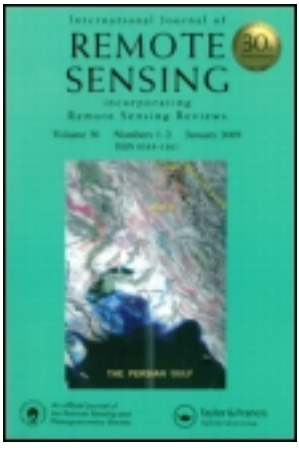

International Journal of Remote Sensing

Publication details, including instructions for authors and subscription information:
http://www.tandfonline.com/loi/tres20

Assessing the impact of cloud morphology on infrared sounder scan geometry

V. Cuomo

Available online: 25 Nov 2010

To cite this article: V. Cuomo (1999): Assessing the impact of cloud morphology on infrared sounder scan geometry, International Journal of Remote Sensing, 20:1, 169-181

To link to this article: http://dx.doi.org/10.1080/014311699213677

INT. J. REMOTE SENSING, 1999, VOL. 20, NO. 1, 169–181

Assessing the impact of cloud morphology on infrared sounder scan geometry

V. CUOMO, C. PIETRAPERTOSA
Istituto di Metodologie Avanzate di Analisi Ambientale, IMAAA/CNR, Tito (Pz), Italy

C. SERIO† and V. TRAMUTOLI
Dipartimento di Ingegneria e Fisica dell'Ambiente, Universitá della Basilicata, Via della Tecnica 3, 85100 Potenza, Italy; e-mail: serio@unibas.it

(*Received 28 October 1996; in final form 18 November 1997*)

Abstract. Next generation infrared sounders from satellites are expected to provide temperature and moisture soundings with an improved vertical resolution. However, this goal could be severely limited by clouds, since infrared sounders are not able to sense through dense clouds. This paper examines the impact of cloud morphology on the scan geometry. More specifically, the problem of how many clear soundings can be achieved, in cloudy areas, as a function of the scan geometry has been addressed. The analysis is particularly devoted to frontal cloud systems which are typically associated with active weather phenomena. These systems are characterized by many spatial scales and result in fractal structures. This particular geometry has been exploited to formulate and check a power law for the dependence of the probability of achieving a clear sounding on the size of the field of view of the sounder. Six Advanced Very High Resolution Radiometer (AVHRR) scenes over north Europe form the basis of our database and various scan geometries, including mono-pixel and multi-pixel configurations, have been analysed.

1. Introduction

Next generation sounding instruments on board operational weather and climate satellites will dramatically improve the vertical resolution and accuracy of temperature and water vapour profiles. Both simulation studies (Kaplan *et al.* 1977, Smith *et al.* 1991 and references therein, Amato *et al.* 1995) and airborne experiments (Smith *et al.* 1988) have shown that accuracies of $\approx 1\,\mathrm{K\,km^{-1}}$ for temperature and 5–10% for water vapour (at least in the lower layers of the troposphere) can be achieved provided that the spectral resolution and the spectral observation density of new sounders improve by 1–2 orders of magnitude over the current satellite systems. However this potential improved performance could be frustrated by the inability of infrared (IR) sounders to sense through dense clouds.

In the past few years much attention has been devoted to the development of inversion schemes which are able to assimilate partly or completely cloudy radiances directly (e.g. Chahine 1974, Susskind *et al.* 1984, Huang and Smith 1986, Eyre 1989).

International Journal of Remote Sensing
ISSN 0143-1161 print/ISSN 1366-5901 online
http://www.tandf.co.uk/JNLS/res.htm
http://www.taylorandfrancis.com/JNLS/res.htm

However, these schemes often rely on simplistic assumptions for the cloud structure which increase the degree of non-uniqueness and uncertainty in the solution of the radiative transfer equation for temperature and water vapour. Thus, new sounders should be designed, within other constraints imposed by the sensor, with a scan geometry and Field of View (FOV) size capable of achieving as many cloud-free soundings as possible.

In this context it should be noted that there are now new cloud clearing methods (e.g. Rizzi *et al.* 1994 and references therein) which rely completely on clear soundings so that improvements in the number and distribution across the scene of clear fields of view may dramatically improve the inversion step to obtain temperature and water vapour profiles from spectral radiances.

A straightforward approach to improve the number of clear soundings in cloudy areas consists of reducing the size of the FOV, since in this way it should be possible to observe through small gaps in broken clouds (Chedin *et al.* 1986). Cuomo *et al.* (1993) used this approach to assess the interrelationship between FOV size and the potential improvement in clear soundings. Their analysis was based on AVHRR (Advanced Very High Resolution Radiometer) data co-located with HIRS/2 (High Resolution Infrared Sounder) radiances. A HIRS/2-like scanning system with FOV sizes ranging from 1 to 40 km was simulated and an exponential improvement in clear soundings was observed as the size of the FOV approached the linear dimension of 1 km. These results are in good agreement with those of Smith *et al.* (1996).

The present study complements the analyses discussed above by considering more possible scanning geometries. In particular the interrelationship between size of the FOV and improvement in clear soundings is discussed for the case of frontal systems. These represent the class of active weather phenomena for which soundings with improved density and quality are really mandatory. In this context, it is commonly recognized that cloud-free IR sounding data on a spatial scale of about 50 km should meet today's requirements of global numerical weather predictions.

2. Data

Our analysis relies on six AVHRR cloud imagery scenes over North Europe which, for simplicity, are referred to as pass A, B, …, F (see table 1). In addition the corresponding cloud masks which were obtained by the cloud detection algorithm operationally running at the Centre de Météorologie Spatiale (Lannion, France, Derrien *et al.* 1993) were used to compute the cloud contamination at each FOV size considered. Figure 1 shows the six passes (brightness temperatures in channel 4) at hand. They include frontal regions of active weather phenomena. In this context the six passes were selected to be representative of weather conditions in which it is considered interesting to improve the quality and density of clear soundings. We

Table 1. Summary of the six overpasses used in our analysis.

Pass	Date	GMT	Orbit	Scan lines
A	17 December 1991	13:29	16635	4782
B	17 December 1991	15:10	16636	4566
C	11 November 1989	03:17	01970	4798
D	12 February 1989	03:07	01984	4881
E	11 February 1989	01:36	01969	4767
F	12 February 1989	13:19	01962	4711

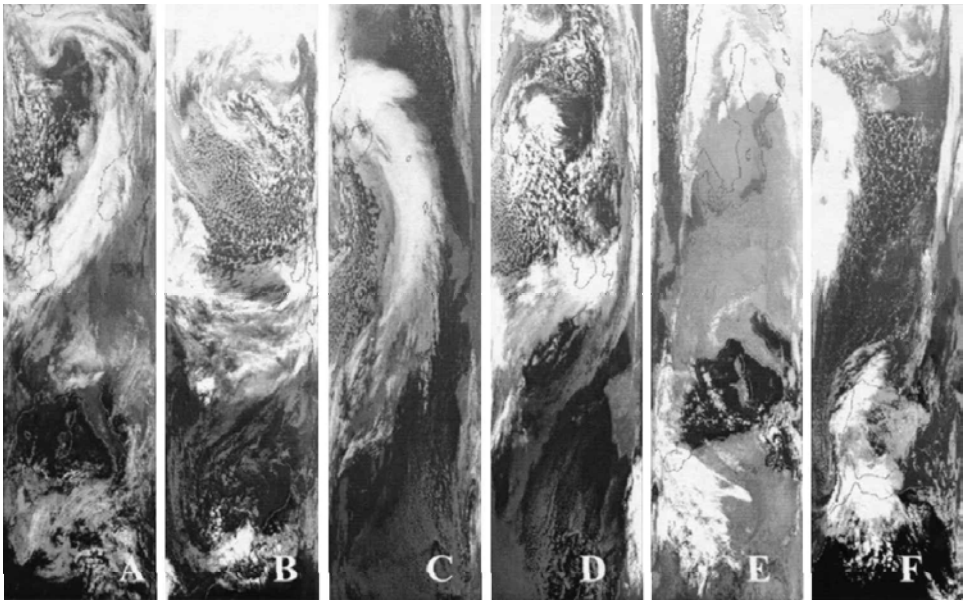

Figure 1. AVHRR channel 4 imagery for passes A, B, C, D, E, F (see table 1).

were not interested in large and compact cloudy areas where no improvement is expected by changing the spatial resolution of the sounder. In the same way we were not interested in cloudy areas which are not associated with active weather phenomena. Finally, we were not interested in large clear areas. These features depend more on the season and latitude, whereas the ability of sensing through gaps in broken clouds depends on the morphology of the cloud system rather than on the statistical distribution of cloud cover over the year.

3. Intercomparing various scan geometries

3.1. *Definition of the scan geometries*

In our analysis the actual HIRS/2 scanning geometry is the basic or reference case. Thus, improvements derived by reducing the FOV size are compared to this reference case. The following two scanning configurations were considered (hereafter referred to as C1 and C2 respectively).

C1. HIRS/2 like scanning with the same number of Fields of View (FOVs) for each scan line and sample spacing as the actual HIRS/2 instrument. The size of the FOV is progressively reduced in order to improve the penetration factor through broken clouds.

C2. Multiple pixel configuration consisting of an array of n by m FOVs where n and m can take various values as will be specified later. The scanning mechanism is assumed to be the same as that for C1, that is the distance between two adjacent scan positions or, in other words, the sample spacing, is constant and set equal to that of the current HIRS/2.

It should be stressed that C1 is assumed to be a mono-pixel configuration. The possible advantage of C2 over C1 is that it should improve the probability of looking through broken clouds because of its multiple FOV configuration.

To understand the details of the two configurations, it should be stressed that our target or sounding area had a size L_H^2 where L_H is the linear HIRS/2 spot size. To simplify the co-location process between each configuration analysed and the AVHRR data, we assume that L_H is equal to 36 in units of the linear AVHRR spot size. Thus the target area contains 36 by 36 resolution elements. With this in mind, in C1 our simulated instrument senses the area L_H by L_H with a single FOV whose linear size can takes the following different values: $L_{C1} = 1, \ldots, 36$, in units of the linear AVHRR spot size. As a consequence, for C1, the sampling density within the target area is constant, that is there is only one sample within the sounding area.

On the contrary, for the composite configuration C2 the sampling density within the target area changes according to the size of the FOV. First, we divide the target area by two and sense the scene by means of two FOVs of linear size $L_{C2} = L_H/\sqrt{2}$ each. This gives the 2×1 configuration. Second, we divide the target area by three and sense the scene by means of three FOVs of linear size $L_H/\sqrt{3}$ each. This gives the configuration 3×1. This procedure is repeated five times to give at each resolution the following five multi-pixel configurations:

- 2×1 geometry, the size of each single FOV is $L_{C2}^2 = L_H^2/2$
- 3×1 geometry, the size of each single FOV is $L_{C2}^2 = L_H^2/3$
- 2×2 geometry, the size of each single FOV is $L_{C2}^2 = L_H^2/4$
- 3×2 geometry, the size of each single FOV is $L_{C2}^2 = L_H^2/6$
- 3×3 geometry, the size of each single FOV is $L_{C2}^2 = L_H^2/9$.

For the sake of clarity the two configurations C_1 and C_2 are summarized schematically in figure 2. To sum up, C1 simply simulates a sensor whose single FOV is progressively reduced while maintaining the sampling density constant within the target area. For C2 the size of the FOV is still progressively reduced but the sampling density is increased accordingly.

3.2. *Defining the clear-sky condition*

Since the AVHRR data are co-located with the simulated FOVs, cloud detection from the AVHRR allows us to establish with high accuracy the amount of cloud coverage at every simulated spot. This cloud coverage is expressed as a number C_c, which takes values from 0 to 100, the latter indicating that the FOV is completely clear. Intermediate values give the fraction of area of the FOV which is cloud-free (e.g. $C_c = 90$ means that 90% of the spot area is clear).

In our analysis two threshold values for C_c were used, 100% and 95%. The last value was considered because it is generally thought that future inversion schemes will be able to deal with slightly cloud-contaminated radiances.

3.3. *Clear air sounding capabilities*

Two indexes were defined in order to assess the capability of each configuration to obtain improved clear soundings. The clearness index N_c measures the fractional amount of clear spots and is computed for each given threshold C_c by:

$$N_c = \frac{\text{number of clear spots}}{\text{total number of spots}} \tag{1}$$

For the multiple FOV configuration C_2 it is possible for more than one of the $n \times m$ pixels to be clear for any given target area or scanning position. However, to compute the index N_c we count up one, for any scanning position, even when the number of

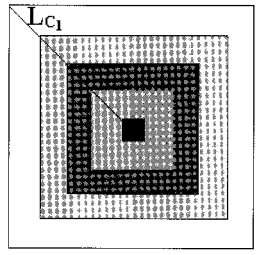

(*a*)

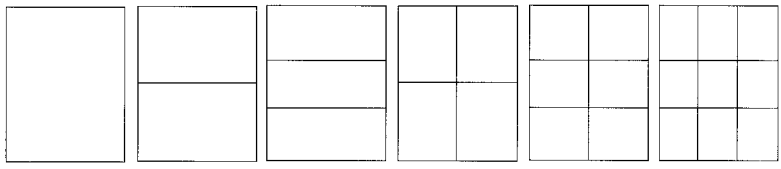

(*b*)

Figure 2. Schematic diagram of the two scanning configurations C_1 (upper part of the figure) and C_2 (lower part of the figure). For C_1 the schematic illustrates how the size of the FOV is progressively reduced. Only a few of the 36 different fields of view (represented as shadowed boxes) are shown. For C_2 the schematic shows the six different multiple configurations which have been used in our analysis (see text for further details).

clear pixels is greater than one. Of course we count up to zero if all the $n \times m$ pixels are cloudy. The logic behind this way of computing N_c is that we can compare this C_2 to C_1 (mono-pixel configuration) more thoroughly and understand whether the supposed difference between the two strategies relies merely on the different sampling density or on an improved probability of obtaining more clear soundings. According to our definitions of N_c if N_c for C_2 is superior to C_1 it means that C_2 improves the penetration factor through broken clouds and hence the probability of obtaining more clear soundings.

The Cluster Index, d_a gives information about the distribution of clear FOVs across the scene. The smaller this index is, the better. It is defined by

$$d_a = \frac{1}{N_{\text{cloudy}}} \sum_{I,J}^{\text{all pixels}} d_{I,J} \tag{2}$$

where $d_{I,J}$, is the distance between pixel (I, J) and the closest clear spot in the scene and N_{cloudy} is the total number of cloudy pixels. Obviously only cloudy pixels contribute to the sum, clear pixels having $d_{I,J} = 0$ by definition. In addition, note that for $N_{\text{cloudy}} = 0$, d_a is not defined (there is no point in defining an index which describes how cloudy FOVs are distributed across a scene when there are no cloudy FOVs at all).

The index d_a provides very important information because uniformly distributed clear FOVs improve the performance of the class of cloud clearing methods which rely mostly on optimal interpolation (e.g. Rizzi *et al.* 1994).

The parameters N_c and d_a have been computed for each scene, FOV size and configuration as defined above. They have been also computed for the HIRS/2 scan geometry. Let N_H and d_H be the clearness and cluster index for the HIRS/2 scan geometry respectively. Then we consider the two normalized indexes:

$$\left\langle \frac{N_c}{N_H} \right\rangle \tag{3a}$$

$$\left\langle \frac{d_a}{d_H} \right\rangle \tag{3b}$$

with the angular brackets denoting expectation. The average is considered over the six different AVHRR scenes. Because of this normalization, the results about the clearness and cluster index can be immediately read as improvements upon the current HIRS/2 spatial resolution.

Figure 3(*a*) shows a plot of the normalized clearness index versus the linear size of the FOV for the threshold $C_c = 100\%$. Note that the curve corresponding to the

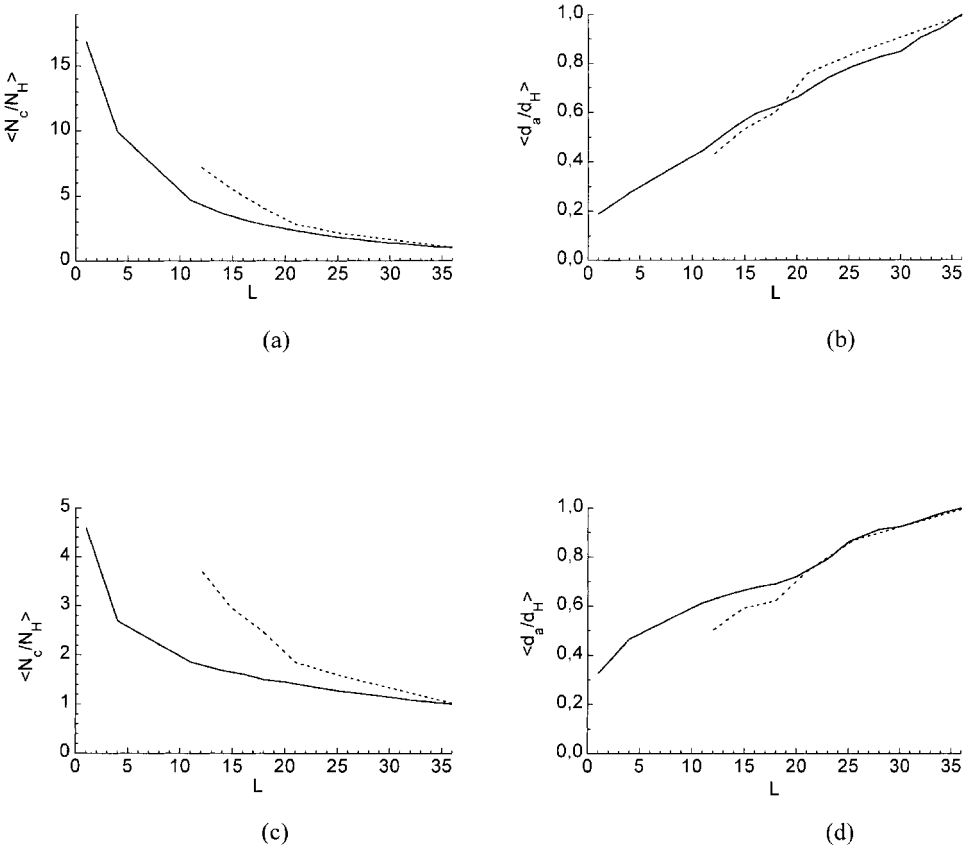

Figure 3. (*a*) Normalized clearness index $\langle N_c/N_H \rangle$, as a function of the linear size of the FOV L (in units of the linear AVHRR spot size 1–36) for the threshold $C_c = 100\%$. (*b*) As (*a*), but for the normalized cluster index $\langle d_a/d_H \rangle$. (*c*) As (*a*) but $C_c = 95\%$. (*d*) As (*b*) but $C_c = 95\%$. In (*a*)–(*d*) the full curves refer to configuration C_1, whereas the dashed curves correspond to C_2.

configuration C2 (broken curve) stops at $L = 12$ km, whereas that for C1 ranges from $L = 1$ to $L = 36$ km. This is because the most resolute geometry for the C2 configuration corresponds to the 3×3 FOV arrangement whose linear spot size is $36/3\,\text{km} = 12\,\text{km}$.

As it is possible to see from figure 3(*a*), by reducing the size of the FOV we achieve a substantial improvement in the probability of producing clear soundings. In general, compared to the mono-FOV configuration, the multi-pixel configuration is superior. This superiority is clearly evident when the sampling density within the target area is greater than 2×2. The 2×2 configuration gives an improvement of a factor about 1·3 as far as the probability of clear soundings is concerned. When the density reaches the level 3×3 the improvement is by a factor of about 1·7.

The superiority of the multiple-FOV configuration is more evident if we consider slight cloud contamination in the FOV, as illustrated in figure 3(*c*) which shows the same plots as in figure 3(*a*) but for $C_c = 95\%$. For the 2×2 configuration the improvement is by a factor of about 1·7, and approximately 2·7 for the 3×3 configuration. However, overall, the advantage over the actual HIRS/2 configuration is less pronounced than in the case corresponding to $C_c = 100\%$.

Note the absence of a relative maximum in all the curves of $\langle N_c/N_H \rangle$ vs L, with L the linear size of the spot. This is characteristic of each scene and is a direct consequence of the many scales which are typical of spatially extended cloud systems.

Figures 3(*b*) and 3(*d*) show plots of $\langle d_a/d_H \rangle$ against the linear size of the spot for the thresholds $C_c = 100\%$ and $C_c = 95\%$ respectively. We see that $\langle d_a/d_H \rangle$ decreases roughly linearly as the spot size becomes small, which indicates that reductions in spot size also improve the clear sounding distribution. However, there is no evident advantage of configuration C2 over C1. Note, again, the absence of relative maxima in the curves.

4. The interrelationship between scale invariance in cloudy areas and the probability of achieving clear soundings

At first glance it seems that the structure of clouds encompasses a large variety of cases and situations which make it impossible to explain or describe their morphology on the basis of simple laws. However, it is now a well established result that atmospheric convection itself tends to produce a particular type of cloud organization that, especially in frontal regions, is scale invariant. In other words the spatial cloud patterns have no intrinsic length scale (Lovejoy 1982, Parker *et al.* 1986, Lovejoy *et al.* 1987, Yano and Takeuchi 1987, Duroure and Guillemet 1990, Weger *et al.* 1992, 1993, Zhu *et al.* 1992, Serio and Tramutoli 1995).

As an example, a well structured cloud pattern is clearly evident in the frontal region of the cloudy system shown in figure 1(*c*). Figure 4(*a*) shows a close up of part of this region (shown in figure 4(*b*)). The scenes displayed in figure 4 consist of brightness–temperature data in the AVHRR channel 4.

Fourier analysis of this image reveals the presence of $1/k^{\alpha}$ noise, that is cross-section power spectra follow a power law of the type $k^{-\alpha}$, with k the wavenumber. Figure 5 shows typical cross-section variance spectra of the cloud system shown in figure 4(*a*). A very definite scaling region extending from wavenumber $k = 0{\cdot}01\,\text{km}^{-1}$ up to $k = 0{\cdot}1\,\text{km}^{-1}$ is clearly visible. From these and similar spectra we estimated an exponent $\alpha \approx 4/3$. A scaling region is also visible beyond $k = 0{\cdot}1\,\text{km}^{-1}$, i.e. to the smallest scales in the field. The scaling exponent is about two for this latter region. The scaling breaking which occurs at about $k = 0{\cdot}1\,\text{km}^{-1}$ suggests that the geometry

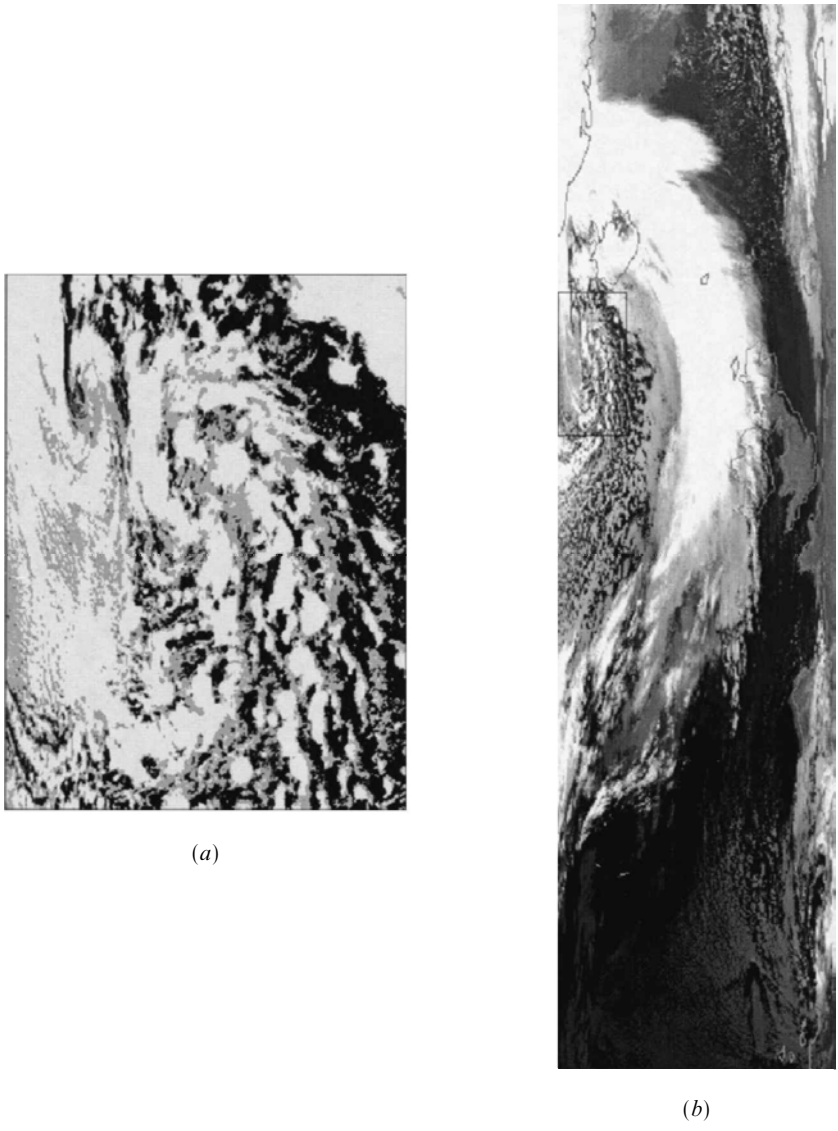

(a) (b)

Figure 4. (a) Close up of the frontal region corresponding to pass C shown in (b). The enlarged region (a) is shown rectangled in (b).

of the cloud pattern, i.e. its correlation characteristics, changes below (above) such a scale. A more detailed scaling analysis performed on the basis of variance diagrams or structure functions (Serio and Tramutoli 1995) shows that below a critical scale, $L_c \approx 18$ km, the field structure is strongly correlated, whereas above such a critical scale the structure of the field becomes strongly anti-correlated. This negative correlation means that at scales greater than 18 km a cloud is likely to be surrounded by a hole and vice versa. Indeed, this anti-correlated character is also evident in figure 4 and from close inspection of the six passes shown in figure 1.

Below the critical scale a positive correlation implies that if we look at the field on the basis of a fine mesh, then it is likely that we explore the structure either of a

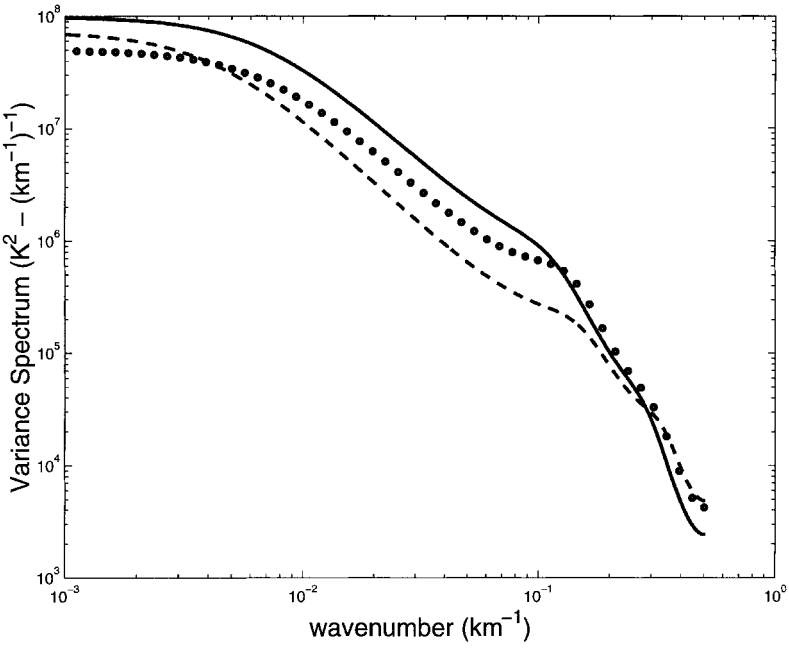

Figure 5. Typical cross-section variance spectra of the cloud system shown in figure 4(*a*).

gap or cloud. However, it must be stressed that the critical scale corresponds only to a change in the correlation structure and not to a maximum in the variance spectra. As a consequence the size of the FOV cannot be optimized simply by making it equal to the critical length. Nevertheless, this size should be at least less than the critical scale, L_c, in order to improve the probability of looking through holes in the cloud pattern.

The absence of any characteristic length scale is evident also from the plots of normalized clearness index against the linear size of the FOV displayed in figure 3. We have already noted the absence of relative maxima in the curves. This behaviour also characterizes the L dependence of the cluster index, d_a, also shown in figure 3.

It is a well known result, originally due to van der Ziel (1950), that the presence of $1/k^{\alpha}$ noise for the spectrum leads to probability distributions in the spatial domain which are themselves power laws. Translated for our case this means that we should expect that the probability $P(L)$ of finding a hole of size greater than L should scale with L, i.e.

$$P(L) \propto L^{-D} \tag{4}$$

where the scaling exponent D is a parameter to be determined. We have checked this result by computing the probability $P(L)$ of observing a clear area of linear size greater than L. The computation was performed for all the six passes shown in figure 1. The results are shown in figure 6 for the threshold value $C_c = 95\%$. The figures show log–log plot of $P(L)$ against L and it is possible to see the presence of a perfect power law.

The power law also applies for different values of C_c although the scaling exponent changes according to the threshold C_c. However, below the critical scale $L_c \approx 20$ km the scaling exponent D is in any case close to 2 which means that by reducing the

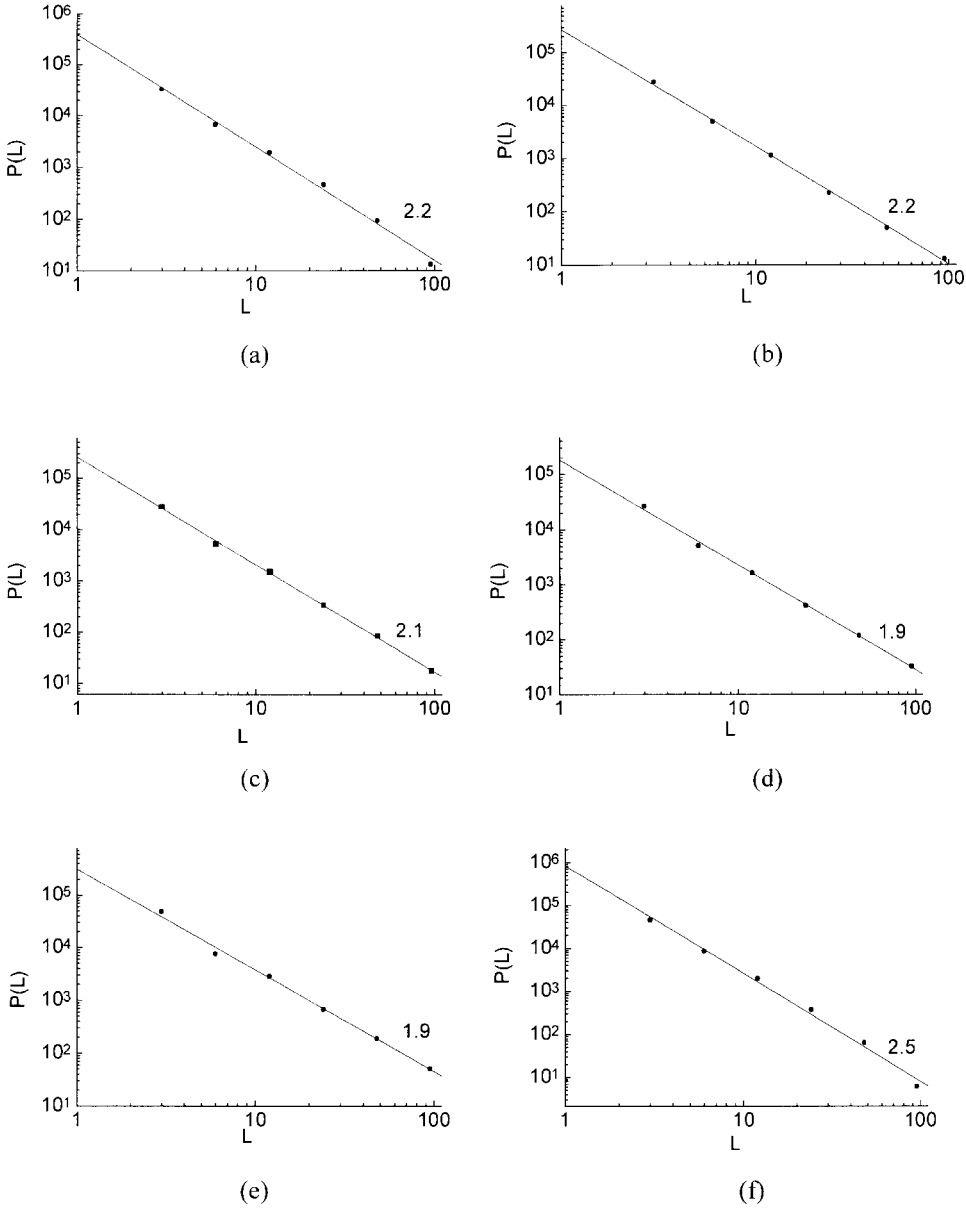

Figure 6. (*a*)–(*f*)plots of $P(L)$ against L for the six passes A to F respectively. The y-axis gives the number of events rather than the normalized probability. The threshold is $C_c = 95\%$. The lines are regression fits to the data and the value of the slope is indicated in the figures.

size of the FOV by a factor of 2 the probability of obtaining a clear area of linear size greater than $L/2$ increases by a factor of 4. Note that the inclusion of slight cloud contamination in the definition of the clear spot masks the presence of the critical scale around 20 km. To appreciate this effect we must use a threshold value $C_c = 100\%$. As an example, figure 7 shows a plot of $P(L)$ against L for pass A and for the case $C_c = 100\%$. Now the change of slope is fairly evident. Furthermore, note

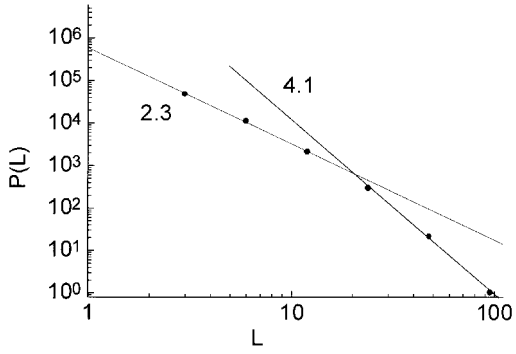

Figure 7. $P(L)$ against L for pass A and $C_c = 100\%$. The two lines are regression fits to the data below and above 20 km respectively. This case illustrates the presence of a critical length scale which is indicated by the change of slope clearly evident in figure (the values of the two different slopes are also indicated on the lines). The slope 4.1 characterizes the data above 20 km, 2.3 is for data below 20 km.

also that below 20 km the characteristic exponent is close to two. Similar results were obtained for all the passes considered in the present analysis.

The change of scale for perfectly clear spots is not surprising: it says that for L which becomes large, the probability of finding a clear hole greater than L drops immediately to zero, much faster than L^{-2} which is the probability law below 20 km. As a consequence, in cloudy regions, there must be a limiting scale above which there are no clear holes at all. Of course, if we allow for cloud contamination, we smooth the cut-off region since we artificially increase the number of clear holes which, in turn, tends to level off the curve $P(L)$ at higher L.

Overall, the findings illustrated here give a good explanation of the data and testify that they are strictly related to the particular self-similar geometry of cloud systems. The self-similarity of cloud systems is the result of atmospheric turbulence, a quite physical and general mechanism governing atmospheric motion. As a result, our findings should apply to any cloud system.

5. Discussion and conclusions

In this paper we have concentrated on analysing the interrelationship between cloud morphology and the characteristic size of holes in broken cloud. This interrelationship has important implications for the optimal design of the FOV geometry of next generation advanced infrared sounders, since a proper design could improve the capability of achieving cloud-free soundings.

The analysis was performed on the basis of AVHRR data from six satellite overpasses over North Europe. This data set allowed us to analyse on a very fine mesh the structure of clouds, especially in frontal systems which are the most interesting to investigate. Different scan geometries were simulated. Both constant and variable sampling densities within a given sounding area were considered. The sounding area was taken to correspond to those of the actual HIRS/2 system and the results are presented directly as potential improvements over the present HIRS/2 capability of achieving clear soundings in cloud systems.

From our analysis it appears that one important, universal, characteristic of cloud morphology dominates the results: *the absence of any dominant length scale* in the cloud patterns associated with frontal systems. Because of this characteristic, the

probability of achieving more and better distributed clear soundings simply improves by: (1) reducing the size of the FOV (the smaller, the better); (2) increasing the sampling density for a given target or sounding area.

This behaviour is thought to be due to the effect of turbulence, which is present in cloud systems associated with active weather phenomena, and therefore it is believed to be universal, that is a general characteristic of frontal systems, independent of season and latitude.

An important consequence is that there is no way of optimizing a scanning geometry characterized by a finite set of scales, since an infinite set of length scales is present in the scenes we want to sense. In other words, the self-similarity of cloud patterns, i.e. the absence of any particular intrinsic scale, leads us to the conclusion that the best performances in terms of clear soundings may only be achieved by considering an imaging system. Only in this way could we reveal all the scales greater than the ultimate scale imposed by the resolution of the imager and therefore resolve all the holes present in the scene above the threshold length imposed by the resolution of the system. This strategy is often referred to as an alias-free scanning mechanism and is, indeed, the mechanism of an imaging system.

However, the presence of a critical length scale at which cloud patterns change correlation structure imposes precise limits to the resolution of an imaging system. The resolution should be better than this critical scale, which from our analysis turns out to be approximately 20 km.

As a consequence of the presence of this small critical scale, at present, an *imaging sounder* does not seem to be a feasible solution because of the associated heavy computational cost and the enormous data rate required.

From our findings, the alternative of an aliased and therefore non-optimal sampling design with an improved density, e.g. 3×3, appears to be more realistic and feasible.

Acknowledgments

This work was supported by the Italian National Space Agency (ASI).

References

Amato, U., Cuomo, V., and Serio, C., 1995, Assessing the impact of radiometric noise on IASI performances. *International Journal of Remote Sensing*, **16,** 2927–2938.

Chahine, M. T., 1974, Remote sensing of cloudy atmospheres. I. The single cloud layer. *Journal of Atmospheric Science*, **31,** 233–243.

Chedin, A., Pick, D. R., Rizzi, R., and Schluessel, P., 1986, Second generation METEOSAT definition studies on microwave and infrared vertical sounders. Technical Report STR-219, European Space Agency, Brussels, Belgium.

Cuomo, V., Serio, C., Tramutoli, V., Pietrapertosa, C., and Romano, F., 1993, Assessing the impact of higher spatial resolution on cloud filtering applied to infrared radiances. *Proceedings of the 7th International TOVS Conference, Igls, Austria, 20–26 February 1994* edited by J. Eyre (Reading: ECMWF), pp. 103–112.

Derrien, M., Farki, B., Harang, L., Le Gleau, H., Noyalet, A., Pochic, D., and Sairouni, A., 1993, Automatic cloud detection applied to NOAA-11/AVHRR imagery. *Remote Sensing of Environment*, **46,** 246–267.

Duroure, C., and Guillemet, B., 1990, Analyze des hétérogénéités spatiales des stratocumulus et cumulus. *Atmospheric Research*, **25,** 331–350.

Eyre, J. R., 1989, Inversion of cloudy satellite soundings radiances by nonlinear optimal estimation: application to TOVS data. *Quarterly Journal of the Royal Meteorological Society*, **115,** 1027–1037.

Huang, H. L. A., and Smith, W. L., 1986, An extension of the simultaneous TOVS retrieval

algorithm with the inclusion of clouds. *Technical Proceedings of the Third International TOVS Study Conference, Madison, Wisconsin, 13–19 August 1986*, edited by P. Menzel (University of Wisconsin: CIMSS), pp. 110–121.

KAPLAN, L. D., CHAHINE, M. T., SUSSKIND, J., and SEARLE, J. E., 1977, Spectral band passes for a high precision satellite sounder. *Applied Optics*, **16,** 322–325.

LOVEJOY, S., 1982, Area–perimeter relation for rain and cloud areas. *Science*, **216,** 185–187.

LOVEJOY, S., SCHERTZER, D., and TSONIS, A. A., 1987, Functional box-counting and multiple elliptical dimensions in rain. *Science*, **235,** 1036–1038.

PARKER, L., WELCH, R. M., and MUSIL, D. J., 1986, Analysis of spatial inhomogeneities in cumulus clouds using high spatial resolution Landsat data. *Journal of Climate and Applied Meteorology*, **25,** 1301–1314.

RIZZI, R., SERIO, C., KELLY, G., TRAMUTOLI, V., MCNALLY, A., and CUOMO, V., 1994, Cloud clearing of infrared radiances. *Journal of Applied Meteorology*, **33,** 179–194.

SERIO, C., and TRAMUTOLI, V., 1995, Scaling laws in baroclinic instabilities. *Fractals*, **3,** 297–314.

SMITH, W. L., WOLF, H. M., HOWELL, H. B., HUANG, H. L., and REVERCOMB, H. E., 1988, The simultaneous retrieval of atmospheric temperature and water vapor profiles—applications to measurements with the high spectral resolution interferometer sounder (HIS) in *RSRM 87: Advances in Remote Sensing Retrieval Methods*, edited by A. Deepak, H. E. Fleming and J. S. Theon (Hampton, VA: Deepak Publishing), pp. 189–202.

SMITH, W. L., WOLF, H. M., HOWELL, H. B., and REVERCOMB, H. E., 1991, Linear simultaneous solution for temperature and absorbing constituent profiles from radiance spectra. *Applied Optics*, **30,** 1117–1123.

SMITH, W. L., HUANG, H. L., and JENNEY, J. A., 1996, An advanced sounder cloud contamination study. *Journal of Applied Meteorology*, **35,** 1249–1255.

SUSSKIND, J., ROSENFIELD, J., REUTER, J., and CHAINE, M. T., 1984, Remote sensing of weather and climate parameters from HIRS-2/MSU on TIROS-N. *Journal of Geophysical Research*, **89,** 4677–4697.

VAN DER ZIEL, A., 1950, On the noise spectra of semi-conductor noise and of flicker effect. *Physica*, **16,** 359.

WEGER, R. C., LEE, J., and WELCH, R. M., 1993, Clustering, randomness, and regularity in cloud fields: 3. The nature and distribution of clusters. *Journal of Geophysical Research*, **98,** (D10), 18449–18463.

WEGER, R. C., LEE, J., ZHU, T., and WELCH, R. M., 1992, Clustering, randomness, and regularity in cloud fields: 1. Theoretical considerations. *Journal of Geophysical Research*, **97,** 20519–20536.

YANO, J. I., and TAKEUCHI, Y., 1987, The self-similarity of horizontal cloud pattern in the intertropical convergence zone. *Journal of the Meteorological Society of Japan*, **65,** 665–667.

ZHU, T., LEE, J., WEGER, R. C., and WELCH, R. M., 1992, Clustering, randomness, and regularity in cloud fields: 2. Cumulus cloud fields. *Journal of Geophysical Research*, **97,** 537–20 558.